Total-Body Multiparametric PET Quantification of ^{18}F-FDG Delivery and Metabolism in the Study of COVID-19 Recovery

Yiran Wang[1,2], Lorenzo Nardo[1], Benjamin A. Spencer[2,1], Yasser G. Abdelhafez[1,3], Elizabeth J. Li[2], Negar Omidvari[2], Abhijit J. Chaudhari[1], Ramsey D. Badawi[1,2], Terry Jones[1], Simon R. Cherry[2,1], Guobao Wang[1]

1. Department of Radiology, University of California Davis Medical Center

2. Department of Biomedical Engineering, University of California, Davis

3. Nuclear Medicine Unit, South Egypt Cancer Institute, Assiut University, Egypt

First and corresponding author: Yiran Wang, 4860 Y Street, Sacramento, CA 95817, Email: yrdwang@ucdavis.edu, Phone: 530-601-3871

Disclaimer: None.

Financial support: NIH grants R01 CA206187, R01 DK124803 and R01 AR076088.

Word count: 5551.

Running title: Total-body parametric FDG-PET of COVID

ABSTRACT

Conventional whole-body ^{18}F-FDG PET imaging provides a semi-quantitative evaluation of overall glucose metabolism without gaining insight into the specific transport and metabolic steps. Here we demonstrate the ability of total-body multiparametric ^{18}F-FDG PET to quantitatively evaluate glucose metabolism using macroparametric quantification and assess specific glucose delivery and phosphorylation processes using microparametric quantification for studying recovery from coronavirus disease 2019 (COVID-19). **Methods:** The study included thirteen healthy subjects and twelve recovering COVID-19 subjects within eight weeks of confirmed diagnosis. Each subject had a dynamic ^{18}F-FDG scan on the uEXPLORER total-body PET/CT system for one hour. Semiquantitative standardized uptake value (SUV) and SUV ratio relative to blood (SUVR) were calculated for regions of interest (ROIs) in different organs to measure glucose utilization. Tracer kinetic modeling was performed to quantify microparametric rate constants K_1 and k_3 that characterize ^{18}F-FDG blood-to-tissue delivery and intracellular phosphorylation, respectively, and a macroparameter K_i that represents ^{18}F-FDG net influx rate. Statistical tests were performed to examine differences between the healthy controls and recovering COVID-19 subjects. Impact of COVID-19 vaccination was investigated. We further generated parametric images to confirm the ROI-based analysis. **Results:** We detected no significant difference in lung SUV but significantly higher lung SUVR and K_i in the recovering COVID-19 subjects, indicating an improved sensitivity of kinetic quantification for detecting the difference in glucose metabolism. A significant difference was also observed in the lungs with the phosphorylation rate k_3, but not with the delivery rate K_1, which suggests it is glucose phosphorylation, not glucose delivery, that drives the observed difference of glucose metabolism in the lungs. Meanwhile, there was no or little difference in bone

marrow metabolism measured with SUV, SUVR and K_i, but a significant increase in bone-marrow ^{18}F-FDG delivery rate K_1 in the COVID-19 group ($p < 0.05$), revealing a difference of glucose delivery in this immune-related organ. The observed differences were lower or similar in vaccinated COVID-19 subjects as compared to unvaccinated ones. The organ ROI-based findings were further supported by parametric images. **Conclusions:** Higher lung glucose metabolism and bone-marrow glucose delivery were observed with total-body multiparametric ^{18}F-FDG PET in recovering COVID-19 subjects as compared to healthy subjects, which suggests continued inflammation due to COVID-19 during the early stages of recovery. Total-body multiparametric PET of ^{18}F-FDG delivery and metabolism can provide a more sensitive tool and more insights than conventional static whole-body ^{18}F-FDG imaging to evaluate metabolic changes in systemic diseases such as COVID-19.

Key Words: ^{18}F-FDG PET; tracer kinetic modeling; total-body dynamic PET; COVID-19.

INTRODUCTION

Positron emission tomography (PET) with the radiotracer ^{18}F-fluorodeoxyglucose (^{18}F-FDG) is a non-invasive *in vivo* molecular imaging technique that reflects glucose metabolism. Conventional whole-body static ^{18}F-FDG PET imaging can provide an overall evaluation of glucose utilization throughout the body, but it mixes the specific glucose transport and metabolic steps. Identification and quantification of these specific processes separately require a fast dynamic scanning protocol, which is however limited to a single organ or a confined region by a conventional short axial field-of-view PET scanner. The advent of total-body PET/CT systems such as uEXPLORER (*1*) and other

long-axial field-of-view PET scanners (*2*,*3*) has brought new opportunities for total-body dynamic PET imaging with increased detection sensitivity and simultaneous dynamic imaging of multiple organs (*4*). Combined with tracer kinetic modeling (*5*), total-body dynamic ^{18}F-FDG-PET enables a multiparametric quantification method (*6*) that allows quantitative measurement of not only overall glucose utilization, but also the microparametric rates of glucose delivery and phosphorylation (*7*) over the entire body.

Though mostly used in oncology, ^{18}F-FDG PET also has the potential for characterizing inflammatory diseases such as vasculitis (*8*), hepatitis (*9*), osteomyelitis (*10*), and recently Coronavirus Disease 2019 (COVID-19) (*11*). COVID-19 primarily attacks the respiratory system, leading to conditions varying from mild manifestations to high-mortality acute symptoms (*12*). Meanwhile, it can affect multiple organs associated with different body systems, including the nervous (*13*), cardiovascular (*14*), and immune systems (*15*). In addition, a variety of prolonged effects of COVID-19 have been reported (*16–19*). However, investigations of the whole-body consequences and prolonged effects from COVID-19 are limited, partially due to the lack of an approach for in-depth total-body evaluation.

In this paper, we conducted a quantitative evaluation of glucose utilization in multiple organs of healthy and recovering COVID-19 subjects using total-body multiparametric ^{18}F-FDG PET imaging. We analyzed the overall glucose metabolism, and more subtly, the blood-to-tissue glucose delivery and glucose phosphorylation to gain further insight into the metabolic differences induced by COVID-19.

MATERIALS AND METHODS

Study Participants and Data Acquisition

With Institutional Review Board approval and written informed consent at the University of California Davis Health, the study includes a cohort of thirteen healthy subjects (all scanned prior to the onset of the COVID-19 pandemic) and twelve COVID-19 subjects. These COVID-19 subjects had mild to moderate symptoms and none of them was hospitalized. Each subject had a total-body one-hour ^{18}F-FDG dynamic scan on the 2-meter long uEXPLORER PET/CT system (*20*,*21*). The PET/CT scans for the COVID-19 subjects were performed within eight weeks of confirmed diagnosis. All COVID-19 subjects tested negative for COVID-19 least two weeks prior to the PET scan. The subjects were injected with 333 ± 45 MBq ^{18}F-FDG intravenously immediately after initiating list-mode data acquisition. A total-body ultralow-dose CT scan (140 kVp, 5 mAs) was performed before the PET scan for attenuation correction. Dynamic PET data were reconstructed into 29 frames (6×10 s, 2×30 s, 6×60 s, 5×120 s, 4×180 s, 6×300 s) with a voxel size of $4 \times 4 \times 4$ mm^3 using the vendor-provided ordered subset expectation maximization algorithm with four iterations and 20 subsets (*20*).

Total-body Kinetic Modeling

Regions of interest (ROIs) were placed in various organs and tissues (e.g., brain, liver, lungs, spleen, bone marrow) throughout the entire body on the dynamic images of each subject (see details of ROI placement in Supplemental Table 1). Time-activity curves (TACs) were then extracted from the organ ROIs. In addition, ROI placement and TAC extraction were also done for the ascending aorta (AA) and right ventricle (RV) to acquire image-derived input functions (IDIFs).

A two-tissue irreversible (2Ti) compartmental model was used for modeling the dynamic ^{18}F-FDG data (*6*) (Supplemental Fig. 1) following a set of differential equations:

$$\frac{\mathrm{d}}{\mathrm{d}t}\begin{bmatrix} C_\mathrm{f}(t) \\ C_\mathrm{m}(t) \end{bmatrix} = \begin{bmatrix} -k_2 - k_3 & 0 \\ k_3 & 0 \end{bmatrix}\begin{bmatrix} C_\mathrm{f}(t) \\ C_\mathrm{m}(t) \end{bmatrix} + \begin{bmatrix} K_1 \\ 0 \end{bmatrix} C_\mathrm{p}(t), \qquad \text{Eq. 1}$$

where $C_\mathrm{p}(t)$, $C_\mathrm{f}(t)$, and $C_\mathrm{m}(t)$ are the ^{18}F-FDG concentrations in the blood plasma, tissue free-state ^{18}F-FDG, and tissue phosphorylated ^{18}F-FDG, respectively. K_1 (mL/min/cm^3) and k_2 (min^{-1}) represent the blood-to-tissue and the tissue-to-blood ^{18}F-FDG delivery rate, respectively; k_3 (min^{-1}) is the ^{18}F-FDG phosphorylation rate. This irreversible model assumes negligible ^{18}F-FDG dephosphorylation, i.e., the ^{18}F-FDG dephosphorylation rate k_4 (min^{-1}) is zero.

The activity that can be directly measured with PET is modeled as a combination of the concentrations in blood and tissue,

$$C_\mathrm{T}(t) = (1 - v_\mathrm{b})\big(C_\mathrm{f}(t) + C_\mathrm{m}(t)\big) + v_\mathrm{b}C_\mathrm{wb}(t), \qquad \text{Eq. 2}$$

where v_b is the blood volume fraction and $C_\mathrm{wb}(t)$ is the ^{18}F-FDG concentration in the whole blood that is approximated by $C_\mathrm{p}(t)$. A time delay correction was applied to account for the time difference from where the IDIF is extracted to the arrival in a tissue (*6*), and different image-derived input functions were used as appropriate for the kinetic modeling of different organs. The IDIF for most organs is the ascending aorta TAC:

$$C_\mathrm{p}(t) = C_\mathrm{AA}(t - t_\mathrm{d}), \qquad \text{Eq. 4}$$

except for the lungs for which the IDIF is the right ventricle TAC:

$$C_\mathrm{p,lung}(t) = C_\mathrm{RV}(t - t_\mathrm{d}), \qquad \text{Eq. 3}$$

where t_d (s) is the time delay correction parameter.

All the kinetic parameters including the time delay were jointly estimated through a non-linear least-square fitting method (*6*) with a weighting factor that considers the time length of each frame and nuclear decay (*22*).

Macroparametric and Microparametric Quantification

The macro-parameter K_i, denoting ^{18}F-FDG net influx rate, is commonly used to characterize overall glucose metabolism and is calculated by:

$$K_i = \frac{K_1 k_3}{k_2 + k_3}. \quad \text{Eq. 8}$$

We also applied semi-quantitative standardized uptake value (SUV) (*23*) and SUV ratio relative to blood (SUVR) (*24*) using the last dynamic frame (55-60 min) to evaluate the overall glucose metabolism. RV was used for the lung SUVR calculation, and AA was used for the SUVR calculation of all other organs.

In addition to the measures of overall glucose metabolism by SUV, SUVR, and K_i, we also used the microparameters of the 2Ti kinetic model, specifically the ^{18}F-FDG delivery rate K_1 and phosphorylation rate k_3, to gain insight into the individual molecular processes of glucose utilization. The ability of this microparametric quantification is a feature that distinguishes compartmental modeling from whole-body static imaging or whole-body dynamic imaging with a simplified graphical analysis method (e.g., the Patlak plot).

Statistical Analysis

Statistical analysis in this study was performed using an unpaired, two-tailed T test and the Mann-Whitney U test on SUV, SUVR and parametric PET metrics to investigate metabolic differences in the recovering COVID-19 subjects compared to the healthy controls. In addition, the tests were performed on lung CT ROIs (Supplemental Table 1) for complementary information. Effect of vaccination was also investigated when appropriate using the statistical tests between the vaccinated and the unvaccinated COVID-19 recovering groups to study the potential influence of vaccination (*25,26*). All statistical data analyses were conducted using MATLAB (Mathworks, MA). P-values of less than 0.05 were considered statistically significant.

For organs that demonstrated a difference in the glucose metabolism, the Pearson correlation analysis between K_i and micro-parameters K_1, k_2, and k_3 was also conducted to further understand their association.

Parametric Imaging of COVID-19

In addition to the ROI-based analysis, voxel-wise parametric images were generated for the healthy and the recovering COVID-19 subjects using the 2Ti compartmental model. Kernel smoothing was applied to both the dynamic images and parametric images for noise reduction (*6*). To make the comparison of parametric images more focused on organs of interest, masking was used to visualize individual organs or tissues (e.g., lung or bone marrow) within the parametric images for inter-subject comparisons.

RESULTS

Patient Characteristics

A summary of patient characteristics is provided in Supplemental Table 2. The healthy subjects include six males and seven females with age 49 ± 15 y and weight 82 ± 18 kg. The COVID-19 subjects include three males, nine females with age 41 ± 10 y and weight 84 ± 25 kg. There was no statistical difference between the two groups in age, weight, body mass index (BMI), blood glucose level, or fasting time before the PET scan using the unpaired T test and the U test. In addition, there was no statistical difference in lung CT values and in the SUV of the input function (neither AA nor RV) between the two groups.

Dynamic Images and TACs

Total-body dynamic ^{18}F-FDG PET images of a representative healthy subject and a recovering

COVID-19 subject are shown in Fig. 1A. Fig. 1B shows four examples of the TACs in the form of SUV and SUVR over time. The most notable finding was the increased lung SUVR in the recovering COVID-19 group compared to the healthy group, while the bone marrow SUVR and spleen SUVR of recovering COVID-19 group also tended to be higher.

Comparison of Overall Glucose Utilization in Multiple Organs

Table 1 summarizes the SUV, SUVR, and K_i of the healthy and the recovering COVID-19 groups along with group comparison results for 11 different organ ROIs. There was no significant difference in lung SUV between the two groups ($p > 0.1$) (Fig. 2). However, there was a statistically significant increase of ~120% in lung K_i in the COVID-19 group ($p \approx 0.01$). SUVR showed a difference (~25% increase) but to a lower degree.

Spleen metabolism and bone marrow metabolism also tended to increase, though did not always achieve a statistical significance, as shown in Table 1 and the boxplots in Fig. 2. K_i produced a larger group difference than SUV, while SUVR was comparable to K_i. We did not observe a statistically significant difference with SUV, SUVR, and K_i in other organs (e.g., brain, liver). Based on the above analyses, the lung, bone marrow, and spleen were selected for further study of microparametric quantification.

Microparametric Quantification of the Lungs

Table 2 shows the analysis of microparametric quantification of the lungs. The correlation between each microparameter and lung K_i is also included using all subject data. Neither K_1 nor k_2 detected any group difference ($p > 0.6$). k_3 was much higher in the COVID-19 group ($p < 0.05$), as further shown in Fig. 3A. Also, k_3 had the strongest correlation with K_i ($r = 0.56, p = 0.0035$) among the three microparameters (Fig. 3B), while the correlations of K_1 and k_2 with K_i

were poor ($p > 0.25$). The findings suggested that increased ^{18}F-FDG phosphorylation (as quantified by k_3) might be the main driving factor for the increased lung ^{18}F-FDG metabolism (assessed by K_i) in COVID-19 recovery.

Microparametric Quantification of Bone Marrow

The microparametric quantification results of bone marrow are summarized in Table 3. While bone marrow metabolism did not show a statistical difference between the two groups as measured with SUVR and K_i (Table 1), bone-marrow ^{18}F-FDG delivery rate K_1 was higher in the COVID-19 subjects, as also shown in Fig. 4. The pelvic bone marrow K_1 was ~20% higher in the COVID-19 group than in the healthy group ($p < 0.05$) (Table 3). In comparison, no statistical significances were observed in k_3. In contrast to the results in the lungs, here the bone marrow microparameters K_1, k_2, and k_3 all had strong correlations with K_i with $p < 0.05$, though the correlation of K_1 with K_i remained weaker (Table 3). Similar results were also found in the spine bone marrow.

Microparametric Quantification of the Spleen

Table 4 shows the microparametric quantification results for the spleen. k_3 was ~45% higher in the COVID-19 group (Fig. 5A), while K_1 and k_2 did not show a significant group difference ($p > 0.3$). k_3 correlated the most strongly with K_i ($r = 0.98$, $p < 0.0001$) among the three microparameters (Fig. 5B), indicating that the increased trend in spleen metabolism (represented by SUVR and K_i) was dominated by the increased ^{18}F-FDG phosphorylation. Overall, the observed changes in the spleen were similar to that of the lungs but with a weaker statistical significance.

Effect of Vaccination

Among the COVID-19 subjects, five were unvaccinated and seven were vaccinated prior to their PET scans (Supplemental Table 2). There was no statistical difference in age, BMI, blood sugar level between the unvaccinated and vaccinated COVID-19 subjects ($p > 0.2$). Lung K_i was significantly higher in unvaccinated COVID-19 subjects (0.00114±0.00029 mL/min/cm^3) as compared to healthy subjects (0.00038±0.00033 mL/min/cm^3) with $p < 0.001$, as shown in Fig. 6A. Lung K_i was reduced in vaccinated COVID-19 subjects (0.00062±0.00042 mL/min/cm^3) but still slightly higher than in healthy controls.

Spine bone-marrow K_1 of both unvaccinated and vaccinated COVID-19 subjects were higher than that of healthy subjects (Fig. 6B). But it did not differ significantly between unvaccinated and vaccinated COVID-19 subjects. No statistical effect of vaccination was noted in other organs of recovering COVID-19 subjects.

Parametric Imaging of Recovering COVID-19

Fig. 7 shows the parametric images of the lungs and bone marrow from healthy subjects and COVID-19 subjects. The lung images of SUVR, K_i and k_3 showed enhanced contrast between the healthy and the recovering COVID-19 compared to SUV (Fig. 7A) through visual inspection, supporting the ROI-based analyses. The spine bone marrow (Fig. 7B) and pelvic bone marrow (Supplemental Fig. 2A) images of K_i and K_1 showed increased contrast between the two subjects than SUV. The SUVR and K_i images of the spleen also tended to have higher contrast as compared to the SUV images (Supplemental Fig. 2B). These observations are consistent with the ROI-based findings.

DISCUSSION

In this study, we evaluated the metabolic differences in multiple organs between recovering COVID-19 subjects and healthy controls using total-body dynamic ^{18}F-FDG PET combined with kinetic modeling. We detected increased metabolism using K_i in the lung, while SUV gave no group differentiation (Table 1 and Fig. 2). The inability of SUV to distinguish the groups is likely due to its semi-quantitative nature and being susceptible to confounding factors (*23*). SUVR showed a larger group difference than SUV but did not outperform K_i. These results suggest the power of kinetic quantification for assessing glucose metabolism. The increased lung metabolism (measured by K_i and SUVR) in the COVID-19 group may indicate continued inflammation during the early stages of recovery. Previous dynamic lung ^{18}F-FDG PET studies have associated increased lung K_i with pulmonary inflammation in multiple conditions, such as acute lung injury (*27*) and chronic obstructive pulmonary disease (*28*). Meanwhile, prolonged lung inflammation caused by COVID-19 has also been reported, which can last more than 60 days after infection even for asymptomatic and patients with mild cases (*29*,*30*).

Another advantage of compartmental modeling is microparametric quantification. According to the analysis in the lungs, ^{18}F-FDG phosphorylation rate k_3 is the parameter that was responsible for the healthy *vs.* COVID-19 group difference in K_i (Fig. 3, Fig. 7A) and correlated best with K_i among different microparameters (Table 2). The result implied that increased ^{18}F-FDG phosphorylation may be the main driving factor for increased lung metabolism during the early stages of recovery from COVID-19, while the glucose delivery rate K_1 in the lungs did not differ between COVID-19 and healthy controls (Table 2). These findings are also consistent with previous animal studies that observed k_3 increases in lung inflammation and the association between K_i and k_3 (*27*,*31*).

Bone marrow demonstrated a significant change of K_1 in the recovering COVID-19 group as compared to healthy subjects (Fig. 4, Fig. 7B), but no differences were observed with SUV, SUVR or K_i that reflects the overall ^{18}F-FDG metabolism (Table 1). This result further indicates the importance of microparametric quantification. Bone marrow is essential for immunoregulation and is the origin of immune cells (*32*). Animal studies have reported that bone marrow cells play an important role in the repair of the injured lung during lung inflammation (*33*,*34*). Hence, the increased ^{18}F-FDG delivery represented by K_1 may be associated with immune system response during COVID-19 recovery. Given that ^{18}F-FDG K_1 of liver was also demonstrated to associate with hepatic inflammation in fatty liver disease (*9*,*35*), the interplay between K_1 and inflammation reaction, and the potential of K_1 as a biomarker of disease, are worth more studies to explore its clinical applications.

The spleen tended to have higher metabolism in the COVID-19 group, as represented by K_i or SUVR (Table. 1). This observation is consistent with the splenic ^{18}F-FDG uptake increase reported in previous studies of COVID-19 (*36*) and other infectious diseases (*37*). As an immune organ, the spleen plays an important role in the immune response to COVID-19 (*38*) and the immune response may lead to increased metabolism.

Our study also separated the unvaccinated and vaccinated COVID-19 groups to evaluate the potential effect of vaccination (Fig. 6). The lower lung K_i in the vaccinated group may indicate reduced lung inflammation due to the protection of vaccination. The data also suggest that the observed differences in the lungs and bone marrow between the recovering COVID-19 group and healthy subjects are more likely a direct result of COVID-19, not due to vaccination.

The study has several limitations. The pilot study cohort is relatively small. With an increased

sample size, it may be possible to further observe some group differences that were not statistically significant in the current study. Although there is no statistical difference in age, weight, BMI, and blood sugar level between healthy subjects and recovering COVID-19 subjects, the unpaired age and gender can introduce potential risks of biased observation. The study lacks histopathology or clinical laboratory data to elaborate the reason for the differences in ^{18}F-FDG kinetics between the two groups. The statistical analysis in this pilot study was not corrected for possible family-wise error rate as the focus of this work is on comparing parametric metrics with SUV. Confirmation of the physiologic findings from this study will require a larger sample size with an appropriate correction for multiple comparisons.

Our next steps are to use a similar methodology to study the impact of long COVID-19 on individual subjects. The interplay and correlation of tracer kinetics among different organs will be also studied in the future. In addition, the results from this pilot work suggest future study designs should focus more on immune-related metabolic changes, e.g., by tracking macrophage (*39*) or neutrophil (*40*) or monitoring serum inflammatory factors.

CONCLUSIONS

With total-body multiparametric PET, increased lung ^{18}F-FDG metabolism (measured by K_i) and increased bone-marrow ^{18}F-FDG delivery (measured by K_1) were detected in recovering COVID-19 subjects as compared to healthy subjects. The changes may be associated with continued inflammation and immune response during the early stages of recovery from COVID-19. These findings are otherwise missed or not possible to find if standard SUV measures are used. Total-body multiparametric ^{18}F-FDG PET can be a more sensitive tool than conventional whole-body ^{18}F-

FDG imaging for detecting subtle changes and may be used for studying post-acute sequelae of COVID-19.

DISCLOSURE

This research is supported in part by the National Institutes of Health (NIH) Grants R01 CA206187, R01 DK124803, and R01 AR076088. University of California, Davis has a research agreement and revenue sharing agreement with United Imaging Healthcare. No other potential conflicts of interest relevant to this article exist.

ACKNOWLEDGEMENTS

We gratefully acknowledge the technologists and staff, particularly Lynda E. Painting, of the EXPLORER Molecular Imaging Center (EMIC), for their assistance in patient consent and data acquisition.

KEY POINTS

QUESTION: Compared to standard whole-body ^{18}F-FDG-PET imaging, is there any benefit from using total-body multiparametric ^{18}F-FDG PET for studying COVID-19 recovery?

PERTINENT FINDINGS: Higher ^{18}F-FDG net influx and phosphorylation in the lung and higher ^{18}F-FDG blood-to-tissue delivery in bone marrow were detected in recovering COVID-19 subjects compared to healthy subjects, while no statistical difference was detected using SUV.

IMPLICATIONS FOR PATIENT CARE: Total-body multiparametric ^{18}F-FDG PET may offer a more sensitive tool for quantitative assessment of multi-organ effects in COVID-19 recovery than SUV

and may be used to study long COVID-19.

REFERENCES

1. Cherry SR, Badawi RD, Karp JS, Moses WW, Price P, Jones T. Total-body imaging: Transforming the role of positron emission tomography. *Sci Transl Med*. 2017;9:eaaf6169.

2. Pantel AR, Viswanath V, Daube-Witherspoon ME, et al. PennPET Explorer: Human imaging on a whole-body imager. *J Nucl Med*. 2020;61:144-151.

3. Alberts I, Hünermund J-N, Prenosil G, et al. Clinical performance of long axial field of view PET/CT: a head-to-head intra-individual comparison of the Biograph Vision Quadra with the Biograph Vision PET/CT. *Eur J Nucl Med Mol Imaging*. 2021;48:2395-2404.

4. Wang Y, Li E, Cherry SR, Wang G. Total-body PET kinetic modeling and potential opportunities using deep learning. *PET Clin*. 2021;16:613-625.

5. Carson RE. Tracer kinetic modeling in PET. In: Positron Emission Tomography. London: Springer; 2005:127-159.

6. Wang G, Nardo L, Parikh M, et al. Total-body PET multiparametric imaging of cancer using a voxel-wise strategy of compartmental modeling. *J Nucl Med*. 2022;63:1274-1281.

7. Sundaram SM, Doughty LA, Sereda MW. Location matters: Hexokinase 1 in glucose metabolism and inflammation. *Trends Endocrinol Metab*. 2022;33:665-667.

8. Zerizer I, Tan K, Khan S, et al. Role of FDG-PET and PET/CT in the diagnosis and management of vasculitis. *Eur J Radiol*. 2010;73:504-509.

9. Wang G, Corwin MT, Olson KA, Badawi RD, Sarkar S. Dynamic PET of human liver inflammation: impact of kinetic modeling with optimization-derived dual-blood input function. *Phys Med Biol*. 2018;63:155004.

10. Wenter V, Müller J-P, Albert NL, et al. The diagnostic value of [^{18}F]FDG PET for the detection of chronic osteomyelitis and implant-associated infection. *Eur J Nucl Med Mol Imaging*. 2016;43:749-761.

11. Zou S, Zhu X. FDG PET/CT of COVID-19. *Radiology*. 2020;296:E118-E118.

12. Hu B, Guo H, Zhou P, Shi Z-L. Characteristics of SARS-CoV-2 and COVID-19. *Nat Rev Microbiol*. 2021;19:141-154.

13. Soltani Zangbar H, Gorji A, Ghadiri T. A review on the neurological manifestations of COVID-19 infection: A mechanistic view. *Mol Neurobiol*. 2021;58:536-549.

14. Zaim S, Chong JH, Sankaranarayanan V, Harky A. COVID-19 and multiorgan response. *Curr Probl Cardiol*. 2020;45:100618.

15. Yazdanpanah F, Hamblin MR, Rezaei N. The immune system and COVID-19: Friend or foe? *Life Sci*. 2020;256:117900.

16. Crook H, Raza S, Nowell J, Young M, Edison P. Long covid—mechanisms, risk factors, and management. *BMJ*. July 2021:374.

17. Guedj E, Campion JY, Dudouet P, et al. ^{18}F-FDG brain PET hypometabolism in patients with long COVID. *Eur J Nucl Med Mol Imaging*. 2021;48:2823-2833.

18. Sollini M, Morbelli S, Ciccarelli M, et al. Long COVID hallmarks on [18F]FDG-PET/CT: a case-control study. *Eur J Nucl Med Mol Imaging*. 2021;48:3187-3197.

19. Sollini M, Ciccarelli M, Cecconi M, et al. Vasculitis changes in COVID-19 survivors with persistent symptoms: an [^{18}F]FDG-PET/CT study. *Eur J Nucl Med Mol Imaging*. 2021;48:1460-1466.

20. Spencer BA, Berg E, Schmall JP, et al. Performance evaluation of the uEXPLORER total-body PET/CT scanner based on NEMA NU 2-2018 with additional tests to characterize PET scanners with a long axial field of view. *J Nucl Med*. 2021;62:861-870.

21. Badawi RD, Shi H, Hu P, et al. First Human Imaging Studies with the EXPLORER Total-Body PET Scanner. *J Nucl Med*. 2019;60:299-303.

22. Thiele F, Buchert R. Evaluation of non-uniform weighting in non-linear regression for pharmacokinetic neuroreceptor modelling. *Nucl Med Commun*. 2008;29:179-188.

23. Thie JA. Understanding the standardized uptake value, its methods, and implications for usage. *J Nucl Med*. 2004;45:1431-1434.

24. van den Hoff J, Oehme L, Schramm G, et al. The PET-derived tumor-to-blood standard uptake ratio (SUR) is superior to tumor SUV as a surrogate parameter of the metabolic rate of FDG. *EJNMMI Res*. 2013;3:1-8.

25. McIntosh LJ, Bankier AA, Vijayaraghavan GR, Licho R, Rosen MP. COVID-19 vaccination-related uptake on FDG PET/CT: An emerging dilemma and suggestions for management. *Am J Roentgenol*. 2021;217:975-983.

26. Keshavarz P, Yazdanpanah F, Rafiee F, Mizandari M. Lymphadenopathy following COVID-19 vaccination: Imaging findings review. *Academic Radiology*. 2021;28:1058-1071.

27. de Prost N, Feng Y, Wellman T, et al. ^{18}F-FDG kinetics parameters depend on the mechanism of injury in early experimental acute respiratory distress syndrome. *J Nucl Med*. 2014;55:1871-1877.

28. Subramanian DR, Jenkins L, Edgar R, Quraishi N, Stockley RA, Parr DG. Assessment of

pulmonary neutrophilic inflammation in emphysema by quantitative Positron Emission Tomography. *Am J Respir Crit Care Med*. 2012;186:1125-1132.

29. Doykov I, Hällqvist J, Gilmour KC, Grandjean L, Mills K, Heywood WE. 'The long tail of Covid-19' - The detection of a prolonged inflammatory response after a SARS-CoV-2 infection in asymptomatic and mildly affected patients. *F1000Research*. 2020:1-9.

30. Albano D, Bertagna F, Bertoli M, et al. Incidental findings suggestive of COVID-19 in asymptomatic patients undergoing nuclear medicine procedures in a high-prevalence region. *J Nucl Med*. 2020;61:632-636.

31. Wellman TJ, Winkler T, Costa ELV, et al. Effect of local tidal lung strain on inflammation in normal and lipopolysaccharide-exposed sheep. *Crit Care Med*. 2014;42:e491-e500.

32. Zhao E, Xu H, Wang L, et al. Bone marrow and the control of immunity. *Cell Mol Immunol*. 2012;9:11-19.

33. Rojas M, Xu J, Woods CR, et al. Bone marrow–derived mesenchymal stem cells in repair of the injured lung. *Am J Respir Cell Mol Biol*. 2005;33:145-152.

34. Yamada M, Kubo H, Kobayashi S, et al. Bone marrow-derived progenitor cells are important for lung repair after lipopolysaccharide-induced lung injury. *J Immunol*. 2004;172:1266-1272.

35. Sarkar S, Corwin MT, Olson KA, et al. Pilot study to diagnose nonalcoholic steatohepatitis with dynamic ^{18}F-FDG PET. *Am J Roentgenol*. 2019;212:529-537.

36. Dietz M, Chironi G, Claessens Y-E, et al. COVID-19 pneumonia: relationship between inflammation assessed by whole-body FDG PET/CT and short-term clinical outcome. *Eur J Nucl Med Mol Imaging*. 2021;48:260-268.

37. Liu Y. Clinical significance of diffusely increased splenic uptake on FDG-PET. *Nucl Med Commun*. 2009;30:763-769.

38. Kaneko N, Kuo H-H, Boucau J, et al. Loss of Bcl-6-expressing T follicular helper cells and germinal centers in COVID-19. *Cell*. 2020;183:143-157.e13.

39. Kim EJ, Kim S, Seo HS, et al. Novel PET imaging of atherosclerosis with ^{68} Ga-labeled NOTA-neomannosylated human serum albumin. *J Nucl Med*. 2016;57:1792-1797.

40. Antoni G, Lubberink M, Sörensen J, et al. In vivo visualization and quantification of neutrophil elastase in lungs of COVID-19 patients: A first-in-humans PET study with ^{11}C-NES. *J Nucl Med*. 2023;64:145-148.

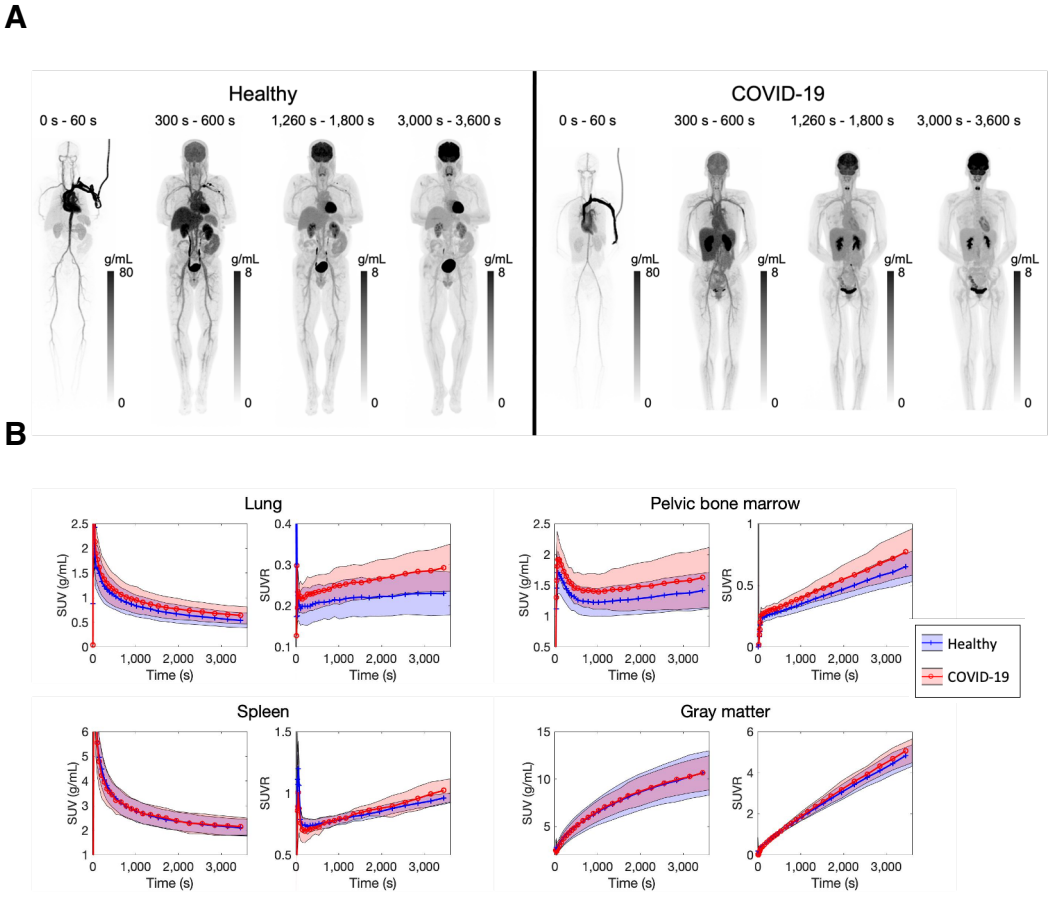

FIGURE 1. (A) Total-body dynamic ^{18}F-FDG PET images of a healthy subject and a recovering COVID-19 subject. Shown are maximum intensity projections. (B) Averaged TACs (shown as SUV and SUVR) of four organs of interest (lung, pelvic bone marrow, spleen, and gray matter) of the thirteen healthy and the twelve recovering COVID-19 subjects. The averaged values are shown as the solid lines, and the standard deviations are shown as the bands.

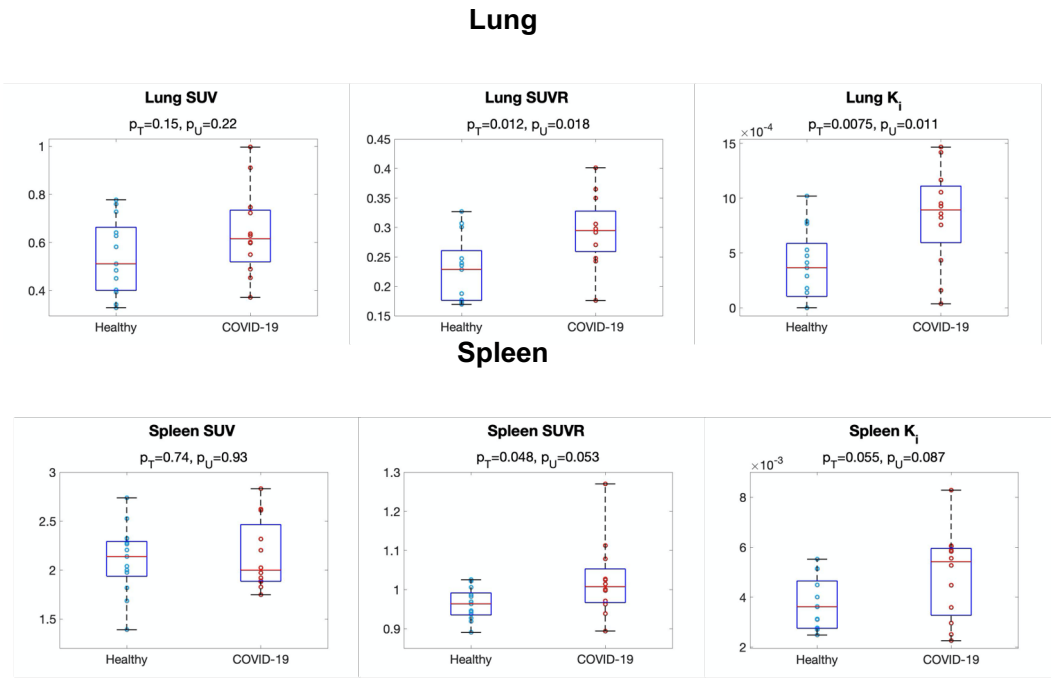

FIGURE 2. Comparison of ^{18}F-FDG glucose metabolism in the lung (top) and spleen (bottom) between the healthy and recovering COVID-19 groups using SUV, SUVR (both at 55 - 60 min), and K_i. p_T and p_U are the p-values of the T test and the Mann-Whitney U test, respectively.

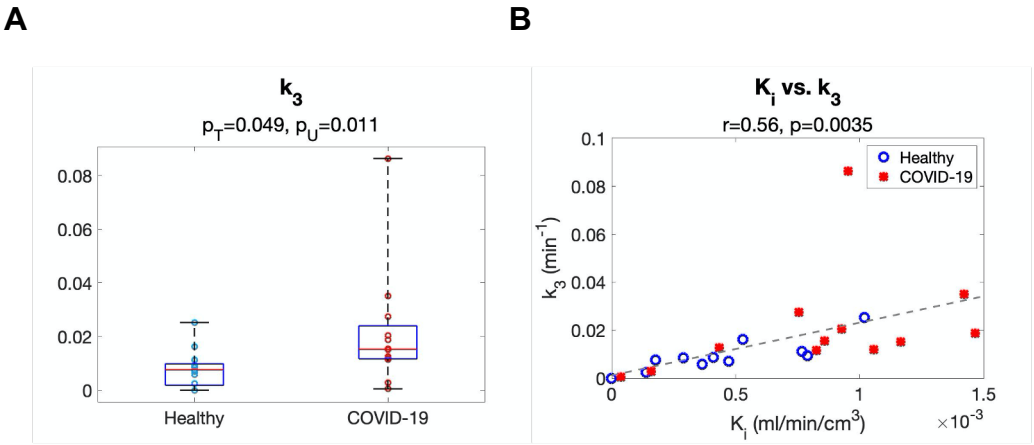

FIGURE 3. Study of lung kinetic parameters in the healthy and the recovering COVID-19 groups. (A) Comparison of ^{18}F-FDG phosphorylation rate k_3 between the two groups. (B) Correlation between k_3 and ^{18}F-FDG net influx rate K_i among the subjects.

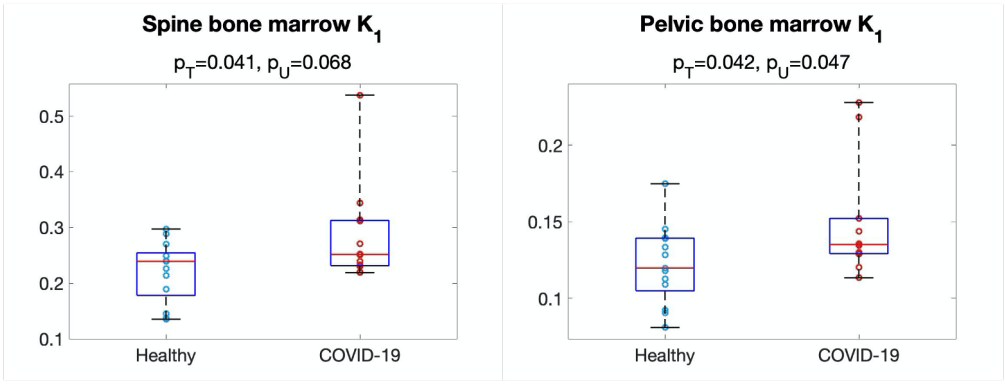

FIGURE 4. Comparison of ^{18}F-FDG delivery rate K_1 of the (A) spine bone marrow and (B) pelvic bone marrow between the healthy and the recovering COVID-19 groups.

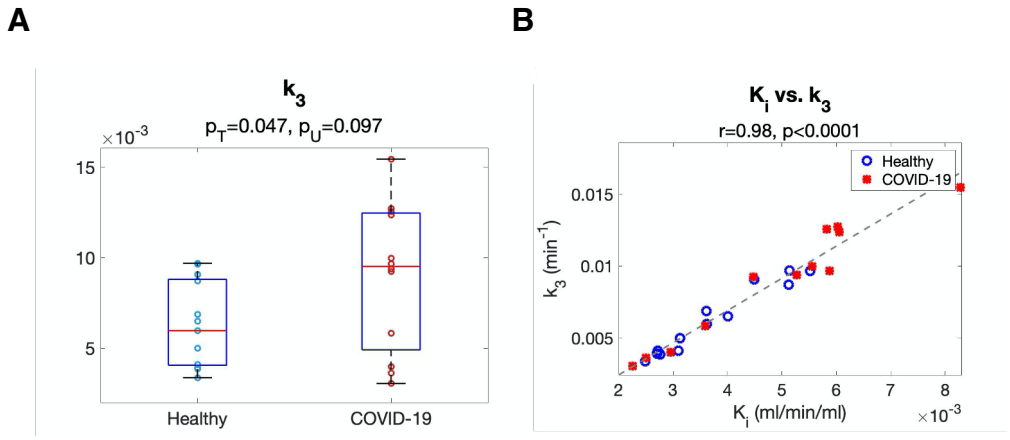

FIGURE 5. Study of microparametric quantification in the spleen. (A) Comparison of k_3 between the two groups. (B) Correlation between k_3 and K_i among the subjects.

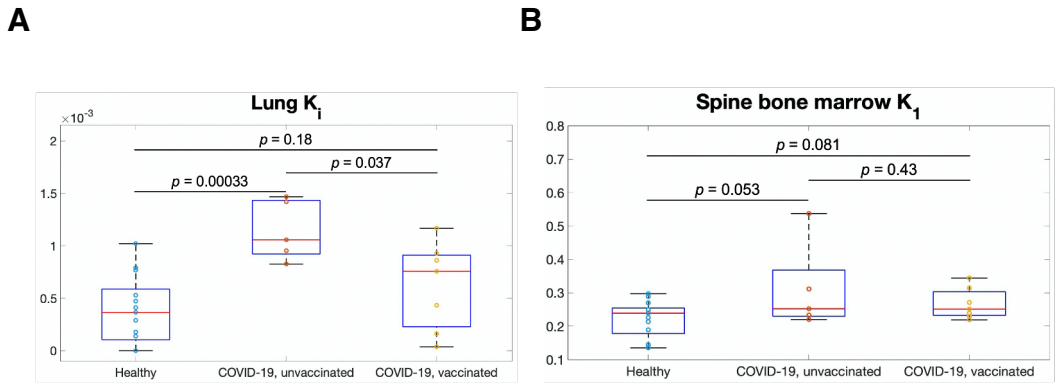

FIGURE 6. Evaluation of unvaccinated and vaccinated COVID-19 subjects as compared to healthy subjects. (A) Lung ^{18}F-FDG net influx rate K_i. (B) Spine bone-marrow ^{18}F-FDG delivery rate K_1. P values were calculated using the unpaired T test.

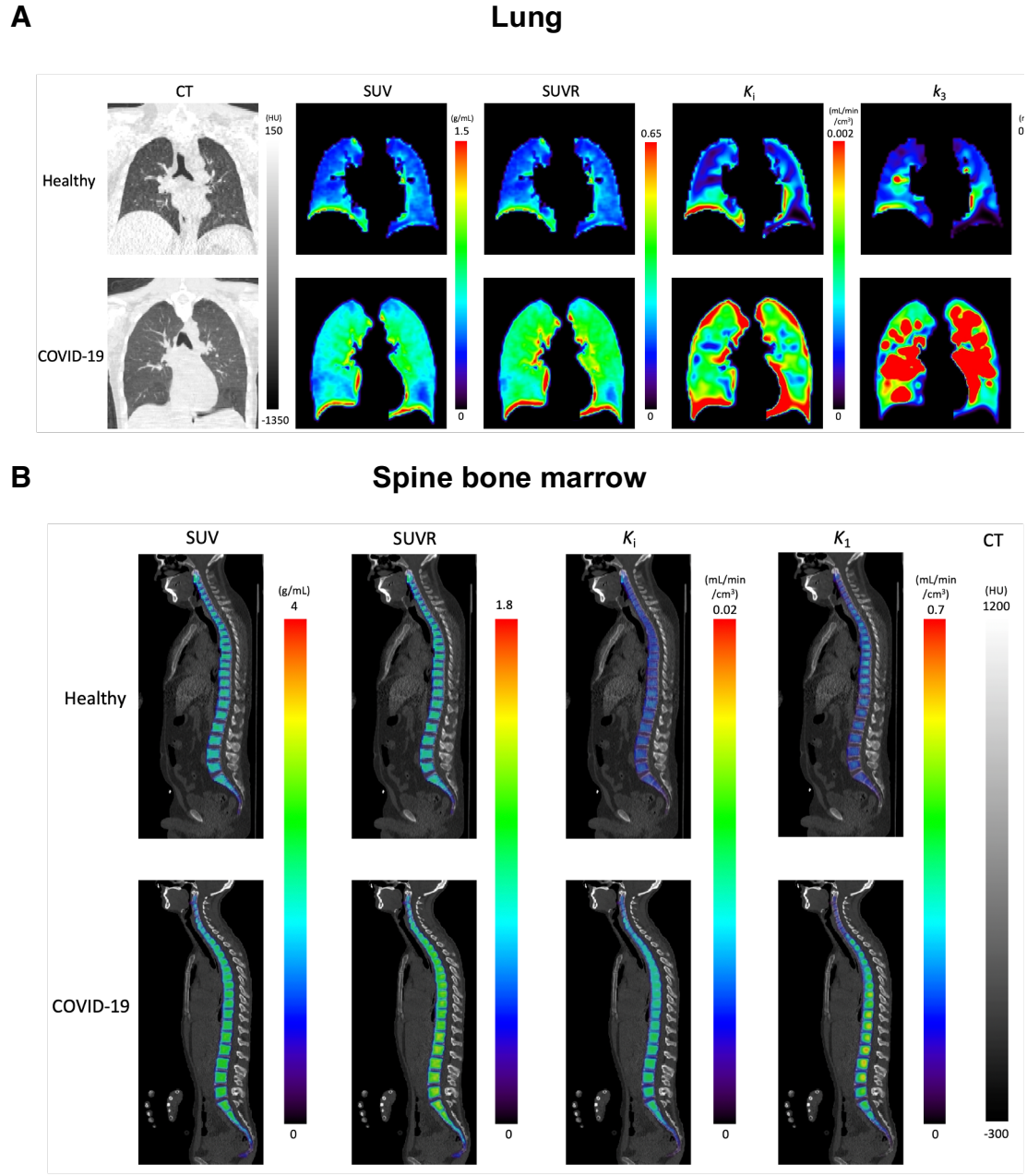

FIGURE 7. Parametric images of example healthy subjects and COVID-19 subjects. (A) Lung CT, ^{18}F-FDG SUV, SUVR, and parametric images of ^{18}F-FDG net influx rate K_i, and ^{18}F-FDG phosphorylation rate k_3. The coronal slices are selected as the mid of trachea carina. (B) Spine bone marrow images of ^{18}F-FDG SUV, SUVR, and parametric images ^{18}F-FDG net influx rate K_i, and blood-to-tissue ^{18}F-FDG delivery rate K_1. The PET images are masked for the bone marrow region and overlaid on the CT images.

TABLE 1

Comparison of the ^{18}F-FDG metabolic metrics SUV, SUVR, and K_i between the healthy subjects and recovering COVID-19 subjects in multiple organs/tissues.

Organ/tissue	Metric	Healthy group (mean ± sd)	COVID-19 recovering group (mean ± sd)	p_T	p_U
Lung	SUV (g/mL)	0.54±0.16	0.64±0.18	0.15	0.22
	SUVR	0.230±0.055	0.293±0.060	0.012	0.018
	K_i (mL/min/cm^3)	0.00038±0.00033	0.00084±0.00045	0.0075	0.011
Myocardium	SUV (g/mL)	7.5±3.5	5.8±2.8	0.21	0.20
	SUVR	3.4±1.6	2.8±1.4	0.38	0.34
	K_i (mL/min/cm^3)	0.055±0.033	0.043±0.025	0.31	0.37
Liver	SUV (g/mL)	2.64±0.44	2.56±0.40	0.65	0.61
	SUVR	1.208±0.060	1.218±0.061	0.69	0.68
	K_i (mL/min/cm^3)	0.00279±0.00094	0.00330±0.00086	0.17	0.17
Spleen	SUV (g/mL)	2.11±0.35	2.15±0.36	0.74	0.93
	SUVR	0.963±0.041	1.024±0.097	0.048	0.053
	K_i (mL/min/cm^3)	0.0037±0.0010	0.0049±0.0018	0.055	0.087
Spine bone marrow	SUV (g/mL)	2.06±0.38	2.21±0.59	0.43	0.57
	SUVR	0.95±0.17	1.05±0.21	0.21	0.22
	K_i (mL/min/cm^3)	0.0072±0.0015	0.0080±0.0023	0.35	0.50
Pelvic bone marrow	SUV (g/mL)	1.42±0.31	1.63±0.51	0.22	0.43
	SUVR	0.65±0.13	0.77±0.20	0.087	0.13
	K_i (mL/min/cm^3)	0.0050±0.0012	0.0059±0.0019	0.19	0.24
Thigh muscle	SUV (g/mL)	0.57±0.16	0.58±0.12	0.92	0.93
	SUVR	0.262±0.056	0.279±0.065	0.50	0.72
	K_i (mL/min/cm^3)	0.00168±0.00057	0.00179±0.00059	0.65	0.89
Gray matter	SUV (g/mL)	10.7±2.4	10.7±1.9	0.99	0.76
	SUVR	4.84±0.54	5.07±0.60	0.33	0.31
	K_i (mL/min/cm^3)	0.0476±0.0062	0.0487±0.0061	0.65	0.68
White matter	SUV (g/mL)	4.5±1.6	3.9±1.0	0.28	0.22
	SUVR	2.03±0.45	1.85±0.31	0.26	0.46
	K_i (mL/min/cm^3)	0.0168±0.0051	0.0148±0.0046	0.33	0.50
Brainstem	SUV (g/mL)	6.1±1.3	5.84±0.82	0.55	0.68
	SUVR	2.78±0.24	2.79±0.34	0.90	0.85
	K_i (mL/min/cm^3)	0.0247±0.0023	0.0241±0.0033	0.62	0.46
Cerebellum	SUV (g/mL)	7.3±1.3	6.99±0.77	0.49	0.50
	SUVR	3.34±0.28	3.35±0.27	0.93	0.89
	K_i (mL/min/cm^3)	0.0300±0.0033	0.0300±0.0030	1.0	1.0

TABLE 2

Healthy *vs.* recovering COVID-19 comparison of lung micro kinetic parameters K_1, k_2, and k_3 and the correlation between the microparameters and lung ^{18}F-FDG net influx rate K_i.

Kinetic parameter	Healthy *vs.* COVID-19 group comparison				Correlation with K_i	
	Healthy group (mean ± sd)	COVID-19 recovering group (mean ± sd)	p_T	p_U	r	p
K_1 (mL/min/cm^3)	0.018±0.022	0.017±0.019	0.89	0.98	0.23	0.26
k_2 (min^{-1})	0.32±0.33	0.26±0.25	0.61	0.81	0.17	0.42
k_3 (min^{-1})	0.0079±0.0071	0.021±0.023	0.049	0.011	0.56	0.0035

TABLE 3

Healthy *vs.* recovering COVID-19 comparison of bone marrow micro kinetic parameters K_1, k_2, and k_3 and the correlation between the microparameters and bone marrow ^{18}F-FDG net influx rate K_i.

Bone marrow type	Kinetic parameter	Healthy *vs.* COVID-19 recovering comparison				Correlation with K_i	
		Healthy group (mean ± sd)	COVID-19 recovering group (mean ± sd)	p_T	p_U	r	p
Spine	K_1 (mL/min/cm^3)	0.221±0.055	0.285±0.089	0.041	0.068	0.46	0.020
	k_2 (min^{-1})	0.76±0.19	0.92±0.31	0.14	0.20	0.45	0.023
	k_3 (min^{-1})	0.0261±0.0061	0.027±0.013	0.73	0.76	0.78	<0.0001
Pelvic	K_1 (mL/min/cm^3)	0.122±0.026	0.149±0.037	0.042	0.047	0.66	0.0003
	k_2 (min^{-1})	0.573±0.081	0.64±0.14	0.17	0.26	0.51	0.0090
	k_3 (min^{-1})	0.0246±0.0060	0.0262±0.0088	0.61	0.81	0.85	<0.0001

TABLE 4

Healthy *vs.* recovering COVID-19 comparison of spleen microparameters K_1, k_2, and k_3 and the correlation between the microparameters and spleen ^{18}F-FDG net influx rate K_i.

Kinetic parameter	Healthy *vs.* COVID-19 group comparison				Correlation with K_i	
	Healthy group (mean ± sd)	COVID-19 recovering group (mean ± sd)	p_T	p_U	r	p
K_1 (mL/min/cm^3)	1.61±0.75	1.31±0.88	0.37	0.40	-0.550	0.0044
k_2 (min^{-1})	2.5±1.0	2.1±1.2	0.34	0.40	-0.426	0.034
k_3 (min^{-1})	0.0062±0.0024	0.0090±0.0041	0.047	0.097	0.98	<0.0001

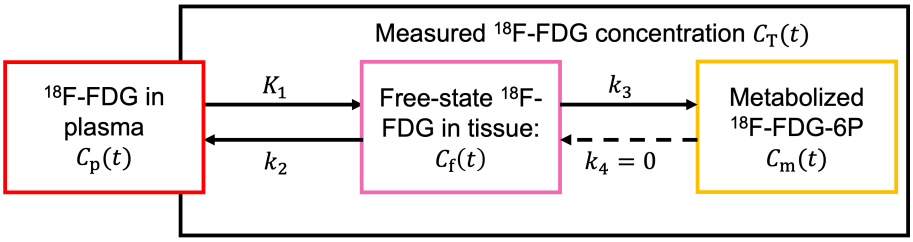

SUPPLEMENTAL FIGURE 1. The tracer kinetics of ^{18}F-FDG is described by a two-tissue irreversible (2Ti) compartmental model.

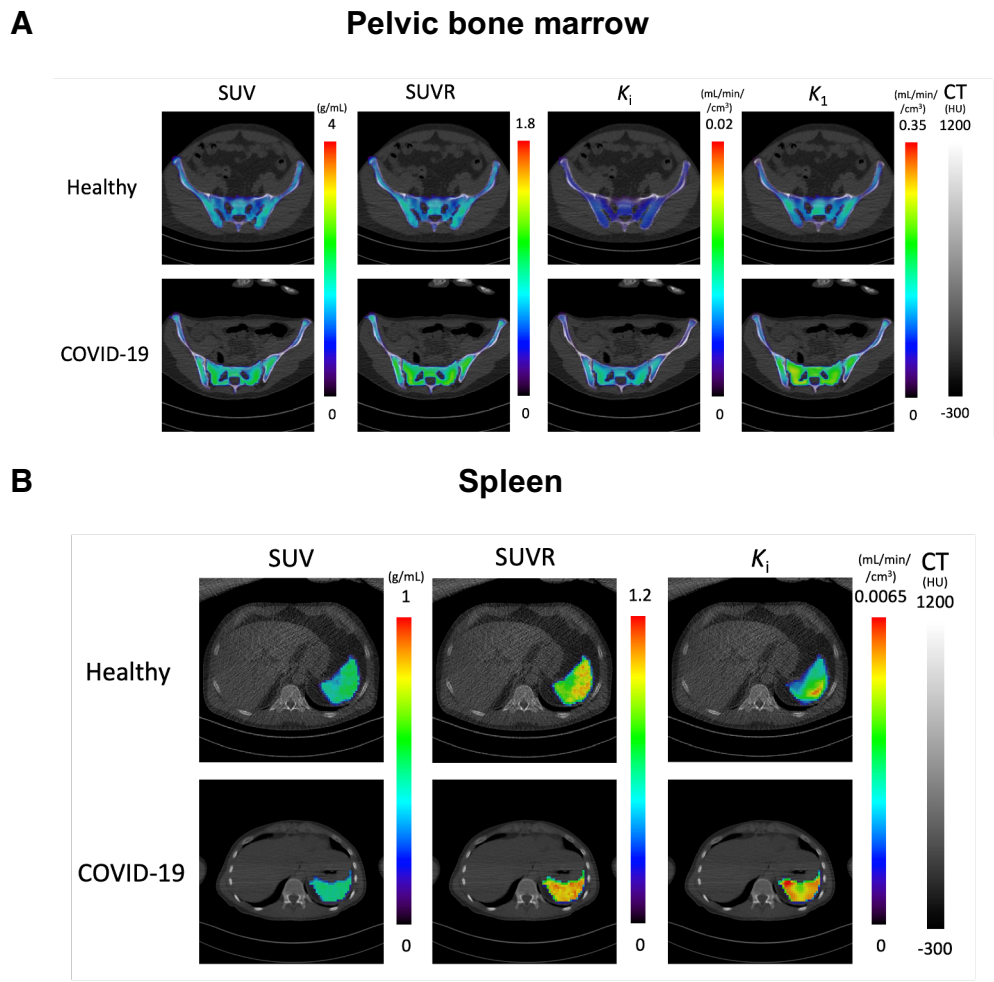

SUPPLEMENTAL FIGURE 2. Parametric images of example healthy subjects and COVID-19 subjects. (A) Pelvic bone-marrow images of ^{18}F-FDG SUV, SUVR, and parametric images of ^{18}F-FDG net influx rate K_i, and blood-to-tissue ^{18}F-FDG delivery rate K_1. (B) Spleen ^{18}F-FDG SUV, SUVR, and parametric images of ^{18}F-FDG net influx rate K_i. The masked PET images are overlaid on the CT images.

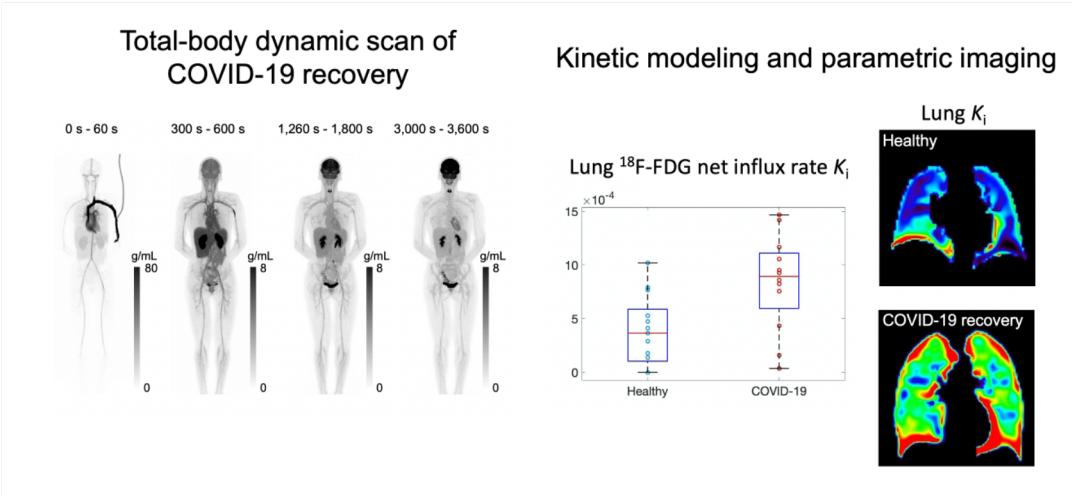

GRAPHICAL ABSTRACT

SUPPLEMENTAL TABLE 1

ROI Placement in Different Organs/Tissues for Kinetic Modelling

Organ/tissue	ROI placement
Lung	Five same-sized spherical ROIs were placed in each of the five lung lobes. Large vessel structures and lung boundary were avoided to minimize the motion effect. The five lobe ROI TACs were extracted and averaged to acquire a global lung TAC.
Myocardium	A 3D free-hand ROI were placed in the myocardium according to both the late frames (45 min - 60 min) and the early frames (0 - 10 min) of the dynamic PET image to minimize the motion and the spill-over effects.
Liver	An ellipsoid ROI was placed in the liver.
Spleen	An ellipsoid ROI was placed carefully in the spleen to diminish the motion effect from the lung.
Spine bone marrow	Ten same-sized cylinder ROIs were placed in the bone marrow of ten spine sections (thoracic T8 - T12, and lumbar L1 - L5). The extracted ten TACs were averaged to acquire a global spine bone TAC. Both PET and CT images were referred.
Pelvic bone marrow	Six ellipsoid ROIs were placed in the pelvic bone marrow, three on the left and three on the right according to both the PET images and CT images.
Thigh muscle	An ellipsoid ROI was placed in the quadriceps femoris muscle of the right thigh and large blood vessels were avoided.
Gray matter	An isocontour ROI was placed in the gray matter according to the late phase (45 min - 60 min) PET image.
White matter	An ellipsoid ROI was placed in the white matter according to the PET image.
Brainstem	An ellipsoid ROI was placed in the brain stem according to the PET image.
Cerebellum	An ellipsoid ROI was placed in the cerebellum according to the PET image
Ascending Aorta	A 3D free-hand ROI was placed according to both the late frames (45 min - 60 min) and the early frames (0 - 10 min) of the dynamic PET images.
Right Ventricle	An ellipsoid ROI was placed according to both the late-frame (45 min - 60 min) and the early-frame (0 - 10 min) dynamic PET images.

SUPPLEMENTAL TABLE 2

Information of individual subjects in the healthy controls and recovering COVID-19 subjects

Subject index	Age (years)	Gender	Weight (kg)	BMI (kg/m^2)	Dose (MBq)	Blood sugar level (mg/dL)	Fasting time before PET scan (hours)	COVID-19 vaccination
H01	76-80	Male	71	24	349	101	11	No
H02	51-55	Female	87	33	389	101	11	No
H03	26-30	Male	112	34	387	77	6	No
H04	46-50	Male	74	27	372	94	12	No
H05	51-55	Female	67	24	348	93	12	No
H06	61-65	Male	88	29	374	92	12	No
H07	61-65	Male	80	24	376	79	12	No
H08	46-50	Male	109	34	370	116	12	No
H09	41-45	Female	53	19	389	78	11	No
H10	51-55	Female	99	36	337	96	12	No
H11	26-30	Female	81	30	370	100	12	No
H12	26-30	Female	58	20	379	79	12	No
H13	51-55	Female	89	35	390	91	10	No
C01	31-35	Female	131	44	303	96	6	No
C02	51-55	Female	106	39	309	86	8	No
C03	41-45	Female	54	20	305	74	10	Yes
C04	46-50	Female	72	29	292	83	12	Yes
C05	36-40	Male	87	25	285	86	10	No
C06	36-40	Female	69	25	298	81	12	No
C07	51-55	Male	87	28	309	93	12	Yes
C08	21-25	Female	59	19	275	74	12	No
C09	46-50	Female	74	30	285	84	7	Yes
C10	46-50	Male	57	19	244	93	12	Yes
C11	26-30	Female	120	43	292	82	10	Yes
C12	41-45	Female	89	31	290	93	12	Yes

Healthy controls are indexed as H01-H13, and COVID-19 recovering subjects are indexed as C01-C12.